CHEMISTRY
A EUROPEAN JOURNAL

DOI: 10.1002/chem.200701562

Heteropoly Acid Encapsulated SBA-15/TiO_2 Nanocomposites and Their Unusual Performance in Acid-Catalysed Organic Transformations

Dhanashri P. Sawant,[a] Josena Justus,[a, b] Veerappan V. Balasubramanian,[a] Katsuhiko Ariga,[a] Pavuluri Srinivasu,[a] Sivan Velmathi,[c] Shivappa B. Halligudi,[a, b] and Ajayan Vinu*[a]

Abstract: The preparation of SBA-15/TiO_2 nanocomposites with different loadings of Keggin-type 12-tungstophosphoric acid (TPA) nanocrystals in their mesochannels through a simple and effective vacuum impregnation method is reported for the first time. The catalysts have been characterised by various sophisticated techniques, including XRD, HRSEM, and TEM. It has been found that the acidity and the textural parameters of the nanocomposites can be controlled by simply changing the loadings of TPA and TiO_2 or the calcination temperature. TPA and TiO_2 loadings of 15 and 22.4 wt%, respectively, and a calcination temperature of 1123 K have proved to be optimal for obtaining mesoporous nanocomposite materials with the highest acidity. Moreover, the activities of these catalysts in promoting hydroamination as well as Mannich and Claisen rearrangement reactions have been extensively investigated. The results show that the amount of TPA has a great influence on the activity of the nanocomposites in all of the reactions studied. The effects of other reaction parameters, such as temperature and reaction time, on the conversion and product selectivity have also been studied in detail. A kinetic analysis of the formation of the products under various reaction conditions is presented. It has been found that the activity of the nanocomposite composed of 15 wt% TPA deposited on 22.4 wt of TiO_2 on SBA-15 in promoting the studied reaction is remarkably higher than the catalytic activities shown by pure TPA, TiO_2-loaded SBA-15, or TPA-loaded SBA-15. The results obtained have indicated that the acidity and the structural control of the nanocomposite materials are highly critical for obtaining excellent catalytic activity, and the presented highly acidic nanocomposites are considered to show great potential for use as catalysts in promoting many acid-catalysed organic transformations.

Keywords: Brønsted acids · mesoporous materials · nanoreactors · nanotechnology · supported catalysts

Introduction

Heteropoly acids have attracted significant attention because of their high acidity and favourable redox behaviour, which make them suitable for applications in size- and shape-selective catalysis. Among the heteropoly acids (HPA), $H_3PW_{12}O_{40}$ is known as a strong acid and has been the focus of considerable attention because it catalyses a variety of organic reactions, such as the alkylation and acylation of hydrocarbons, the hydration of alkenes, and the polymerisation of THF.[1,2] However, this HPA exhibits low surface area (5–10 $m^2 g$), pore volume, and thermal stability, which limit its utility in many catalytic reactions. Thus, the deposition of HPAs having the Keggin structure on porous solid supports with high surface area, large pore diameter, and high specific pore volume is seen as a critical means of improving their properties and obtaining better performance

[a] Dr. D. P. Sawant, J. Justus, Dr. V. V. Balasubramanian, Dr. K. Ariga, Dr. P. Srinivasu, Dr. S. B. Halligudi, Dr. A. Vinu
Nano-ionics Materials Group
National Institute for Materials Science
1-1, Namiki, Tsukuba, 305-0044 (Japan)
Fax: (+81) 29-860-4563
E-mail: vinu.ajayan@nims.go.jp

[b] J. Justus, Dr. S. B. Halligudi
Inorganic Chemistry and Catalysis Division
Department of Catalysis, National Chemical Laboratory
Pune 411008 (India)

[c] Dr. S. Velmathi
National Institute of Technology
Trichirappalli, Tamil Nadu (India)

Supporting information for this article is available on the WWW under http://www.chemeurj.org/ or from the author.

in many potential heterogeneous catalytic applications.[3–5] It has also been demonstrated that the thermal stability of such supported HPAs may be enhanced through judicious choice of the most appropriate porous supports.[6–10] The encapsulation of HPA on many supports, such as carbon,[6] silica,[7] titania,[8] zirconia,[9] and mixed oxides, has been reported; these supports stabilise the Keggin units of the HPAs, which are responsible for providing the acid sites, and as a result the catalytic performances and thermal stabilities of the HPAs in the porous matrices greatly exceed those of the pristine HPAs.[11–13]

Titania (TiO_2) has received considerable attention because of its excellent characteristics, such as chemical stability, non-toxicity, and excellent redox behaviour with mild acidity. Moreover, it also has several other advantages, such as low cost, biocompatibility, and low environmental impact. These properties make it useful for many potential applications, including the production of pigments, catalysts, photocatalysts, solar cells, optical thin-film filters, and so on. However, there are also some disadvantages associated with the use of TiO_2, which include low specific surface area, poor thermal properties, and low mechanical strength. Therefore, in recent years, much effort has been directed towards overcoming these problems by devising new catalyst formulations, whereby the thermal stability of TiO_2 (anatase) is enhanced without compromising its unique physicochemical properties. Recently, tungstophosphoric acid (TPA) supported on TiO_2 has been reported by several researchers as a highly active catalyst for the co-generation of phenol/acetone,[14] for the production of glycol ethers,[15] and for many other transformations.[16–21] The preparation of mesoporous TiO_2 with high surface area and a well-ordered pore structure has also been reported by several research groups. It was demonstrated that this material shows excellent catalytic activity in photocatalysis due to the greater accessibility of the large reactant molecules present inside the mesochannels.[22–24] Moreover, a supported catalyst consisting of TiO_2 nanoparticles on mesoporous silica has been prepared by a wet-impregnation method, and was found to be highly active in promoting many catalytic reactions.[25–28] Unfortunately, the wet-impregnation method is not useful for depositing an amount of heteropoly acid molecules sufficient for the formation of nanocrystals within the porous channels of mesoporous silica materials.[28] Thus, ultra-large pore SBA-15 with very high surface area and a well-ordered pore structure has been utilised as a support for TiO_2. Moreover, a simple and effective vacuum impregnation method has been used to obtain a high loading of TPA therein, which is an essential requirement for the formation of TPA nanocrystals and can enhance the stabilisation of its Keggin units within the mesochannels of the support.

Hydroamination (HA) is a reaction of considerable interest because it offers a very straightforward approach for the synthesis of substituted amines and their derivatives without any by-product formation.[29] Although there have been many reports on the hydroamination of alkynes and allenes over lanthanide,[30,31] early,[32,33] and late transition metal catalysts, a general catalyst for promoting the addition of amines to alkenes remains elusive. Only one process, the synthesis of *tert*-butylamine from ammonia and isobutene, has hitherto been commercialised.[34] The solid-acid-mediated HA of acrylates with amines offers a simple approach to the synthesis of amino acid derivatives that can be used in peptide analogues or as precursors to optically active amino alcohols, diamines, and lactams. Unfortunately, only a few reports dealing with this topic are available in the open literature. These include a report by Sugi and co-workers, who described the HA of acrylates with aromatic amines using zeolites as catalysts.[35]

The Mannich reaction is one of the most important C–C bond-forming reactions in organic synthesis for the preparation of secondary and tertiary amine derivatives.[36] The products of the Mannich reaction are mainly α-amino carbonyl compounds and their derivatives, and these are used for the synthesis of amino alcohols, peptides, and lactams, or as precursors to optically active amino acids. Conventional homogeneous catalysts for classical Mannich reactions of aldehydes, ketones, and amines include organic and mineral acids, such as proline,[37–39] acetic acid,[40] *p*-dodecylbenzenesulfonic acid,[41] and some Lewis acids.[42,43] However, these often suffer from drawbacks of long reaction times, harsh reaction conditions, toxicity, and difficulty in product separation, which limit their use in the synthesis of complex molecules. As a means of overcoming this problem, the development of active heterogeneous catalysts with predefined active sites, obtained by immobilising TPA on insoluble mesoporous silica supports, appears to be a highly promising strategy.

The Claisen rearrangement is another versatile reaction for C–C bond formation in organic synthesis. Although this reaction is traditionally performed under thermal conditions, there has been growing interest in metal-catalysed Claisen rearrangements that may be performed under mild conditions.[44] The Claisen rearrangement[45] of allyl phenyl ethers (APE) to 2-allylphenols (2-AP) is a well-studied reaction, and its extension to the corresponding aza and thia analogues has rendered it more versatile for the synthesis of numerous five- and six-membered oxygen, nitrogen, and sulfur heterocycles through synthetic ramification of the initial rearrangement products.[46] This reaction has been carried out under thermal conditions (453–473 K). Very recently, a variety of Lewis acids, such as $BF_3{\cdot}AcOH$, BCl_3, $Et_2AlCl{\cdot}TiCl_4$, and $(i\mathrm{PrO})_2TiCl_2$, have been employed to accelerate this rearrangement under much milder conditions.[47–50] However, these catalysts are associated with a number of disadvantages, including difficulty of separation from the reaction mixture, toxicity, and lower chemical and mechanical stability. These problems might be overcome by employing suitable highly acidic solid catalysts with high chemical and mechanical stability.

Here, we report the successful preparation of TiO_2-supported mesoporous SBA-15 nanocomposites with different loadings of Keggin-type 12-tungstophosphoric acid (TPA) nanocrystals in their mesochannels through a simple and ef-

fective vacuum impregnation method. The obtained materials have been unambiguously characterised by various sophisticated techniques, including XRD, N_2 adsorption, ^{31}P MAS NMR, HRTEM, FT-IR of adsorbed pyridine, and temperature-programmed desorption of ammonia (NH_3-TPD). The activity and stability of these catalysts in relation to the aforementioned organic transformations have been extensively investigated. The effects of various reaction parameters on conversion and product selectivity have been studied. A kinetic analysis of the formation of the products under various reaction conditions is also presented. It has been found that the activity of TPA encapsulated over TiO_2/SBA-15 is remarkably higher than that of pure TPA, TiO_2/SBA-15, or TPA/SBA-15.

Results and Discussion

Structural characterisation and textural properties of TPA/TiO_2/mesoporous silica materials: The ratio of W to P in 15 wt% TPA/22.4 wt% TiO_2/SBA-15, corresponding to the ratio per Keggin unit, was estimated by EDX, XRF, and ICP-AES analysis as 12.13 and 12.07, respectively, in good agreement with the value for pristine TPA. Small-angle X-ray powder diffraction patterns of these catalysts with different loadings of TPA, calcined at 1123 K, are shown in Figure 1A. As can be seen in Figure 1A, TiO_2/SBA-15 samples with TPA loadings up to 50 wt% exhibit a sharp peak at a low angle and two higher order peaks, which can be indexed to the (100), (110), and (200) of the hexagonal space group *P6mm*. However, the structure of the material is significantly affected as the TPA loading is further increased above 50 wt%.

Wide-angle XRD patterns of TiO_2/SBA-15 with different loadings of TPA are shown in Figure 1B. The samples with TPA loadings of up to 15 wt% exhibit several well-defined peaks characteristic of pure anatase TiO_2 (A-TiO_2), which can be indexed as (101), (004), (200), (105), (211), (204), (116), and (215). This phase is critical for performing organic transformations. When the TPA loading is increased above 15 wt%, peaks corresponding to WO_3 crystallites gradually appear. This can be mainly attributed to the decomposition of TPA molecules into tungsten oxides. In addition, an anatase-to-rutile phase transformation is found for samples with a TPA loading in excess of 50 wt%, revealing that a higher loading of TPA also induces this phase transition of the TiO_2. The mean crystallite sizes of the TiO_2 nanoparticles in the 15T-22.4TO-S15-1123 and 22.4TO-S15-1123 nanocomposites, as estimated from the XRD peak width of (101) using the Scherrer equation, are given in the footnotes to Table 1. It is interesting to note that the crystallite size of the TiO_2 nanoparticles in 15T-22.4TO-S15-1123 is much smaller than that of those in 22.4TO-S15-1123. These observations confirm that the TPA loading of 15 wt%, which forms a covering monolayer on the surface of the nanocomposite and inhibits the agglomeration of the TiO_2 nanoparticles inside the mesochannels, is crucial for stabilisation of the anatase phase and favors the formation of small crystallite size TiO_2 nanoparticles on the 15T-22.4TO-S15-1123 nanocomposite.

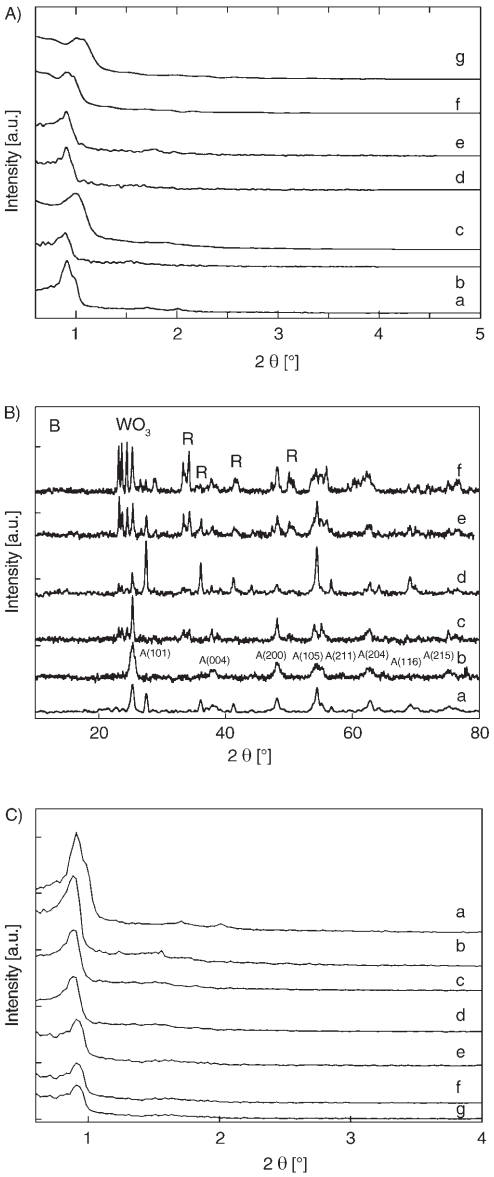

Figure 1. A) Low-angle XRD patterns of a) pure SBA-15, and b)–g) *x*T-22.4TO-S15-1123 with different TPA loadings: b) 5, c) 15, d) 30, e) 50, f) 70, and g) 90 wt.%. B) Wide-angle XRD patterns of *x*T-22.4TO-S15-1123 with different TPA loadings: a) 5, b) 15, c) 30, d) 50, e) 70, and f) 90 wt.%. C) Low-angle XRD patterns of a) pure SBA-15 and b)–g) 15T-22.4TO-S15-*z* calcined at different temperatures: b) 923, c) 1023, d) 1123, e) 1173, f) 1223, g) 1273 K.

To investigate the effect of the calcination temperature on the stability of the TPA and the phase transition of the support, nanocomposites were calcined at different temperatures. Low-angle XRD patterns of 15T-22.4TO-S15-X calcined at different temperatures are shown in Figure 1C. It can be seen from Figure 1C that the calcination temperature plays a critical role in controlling the structure of the support and the phase transition of the TiO_2. Although the low-

Table 1. Physico-chemical properties of the catalysts and their catalytic activities.[a]

Samples	SA [$m^2 g^{-1}$]	PV [$cm^3 g^{-1}$]	PD [Å]	TA [mmol g^{-1}]	B/L	TOF [s^{-1}] $\times 10^{-2}$[b]	RC 10^{-5} [s^{-1}]	Conv. [%]
without catalyst	–	–	–	–	–	–	–	2
22.4TO-S15-1123	403	0.67	71.8	0.28	0.90	–	3.81	24
5T-22.4TO-S15-1123	372	0.61	70.9	0.26	1.00	18.4	4.96	30
15T-22.4TO-S15-1123	353	0.55	68.7	0.38	1.40	11.9	12.05	58
30T-22.4TO-S15-1123	325	0.54	67.8	0.31	1.14	4.2	7.33	41
50T-22.4TO-S15-1123	302	0.50	67.4	0.29	1.09	1.8	4.76	29
70T-22.4TO-S15-1123	190	0.30	66.9	0.24	0.82	0.8	2.93	19
90T-22.4TO-S15-1123	190	0.29	65.5	0.22	0.56	0.4	1.93	13
15T-10TO-S15-1123	395	0.65	71.3	0.26	0.90	13.3	4.76	29
15T-30TO-S15-1123	295	0.44	70.3	0.28	1.13	5.0	5.56	33
15T-50TO-S15-1123	187	0.30	69.6	0.20	1.07	2.0	3.45	22
15T-70TO-S15-1123	165	0.23	69.0	0.19	0.74	0.9	1.93	13
effect of calcination temperature (K) on 15T-22.4TO-S15-z								
873	502	0.65	72.1	–	–	–	–	–
923	462	0.61	71.7	0.22	0.55	2.66	1.93	13
1023	390	0.57	71.3	0.30	1.10	6.13	4.95	30
1173	306	0.44	68.4	0.32	1.17	7.36	6.19	36
1223	228	0.40	67.8	0.23	0.65	5.52	4.37	27
1273	202	0.31	67.1	0.21	0.40	2.25	1.62	11

[a] Entry 2: TiO_2 phase (tetragonal); crystal size by TEM = 5.7–6.7 nm and by XRD = 6.2 nm. Entry 4: TiO_2 phase (tetragonal); crystal size by TEM = 4.5–5.5 nm and by XRD = 4.8 nm. Conditions: aniline (1.45 g, 0.016 mol) + ethyl acrylate (EA) (1.55 g, 0.016 mol), aniline/EA (mol ratio) = 1, catalyst = 0.3 g, T = 383 K, t = 2 h. SA = surface area; PV = pore volume; PD = pore diameter; TA = total acidity; B/L = ratio of Brønsted and Lewis acid sites; TOF = turnover frequency; RC = rate constant; conv. = conversion. [b] TOF is calculated by considering three protons per Keggin unit (mol mol^{-1} H^+ s^{-1}).

angle (100) peak is seen for all of the samples, irrespective of calcination temperature, the intensity of this peak decreases significantly with increasing calcination temperature. Moreover, samples calcined at temperatures up to 1123 K show a sharp peak at a low angle together with several higher order peaks, revealing that the mesostructural order of the support is retained. However, when the calcination temperature is increased above 1123 K, the higher order peaks gradually diminish in intensity, indicating destruction of the mesostructure of the support. It must also be noted that up to a calcination temperature of 1123 K only the anatase phase is formed, whereas the anatase-to-rutile phase transformation occurs when the calcination temperature is increased above 1123 K. Figure S1 shows wide-angle XRD patterns of the catalysts 15T-xTO-S15-1123 with different loadings of TiO_2. It is interesting to note that with TiO_2 loadings of up to 30 wt%, only the anatase phase is formed. However, both the anatase phase and a large amount of the rutile phase are formed when the TiO_2 loading exceeds 30 wt%. These results indicate that the 22.4 wt% loading of TiO_2 is the optimum amount for obtaining only the anatase phase in the 15T-xTO-S15 nanocomposites.

To investigate the effects of calcination temperature and the loadings of TPA and TiO_2 on SBA-15 on the textural parameters, the samples were characterised by nitrogen adsorption–desorption isotherms. The textural properties of T-TO-S15-1123, with different loadings of TPA and TiO_2, and of 15T-22.4TO-S15-X, calcined at different temperatures, are presented in Table 1. It is noteworthy that the textural parameters of the T-TO-S15 nanocomposites are significantly affected by the modification. It is evident that the specific pore volume and the specific surface area of the modified samples are much lower compared to those of the parent SBA-15, and decrease with increasing TPA or TiO_2 loadings. This reduction in the surface area and pore volume after modification could be due to the fact that the TPA and TiO_2 are deposited inside the mesochannels and are well-dispersed on the surface of the hexagonally ordered mesoporous SBA-15 support. It can be seen from Table 1 that the specific surface areas of the samples with TPA loadings of up to 50 wt% are in excess of 300 $m^2 g^{-1}$, and that their pore volumes are in the range 0.50–0.61 $cm^3 g^{-1}$, which satisfy the requirements for catalytic action. The specific surface area is 372 $m^2 g$ for 5T-22.4TO-S15-1123 and decreases to 190 $m^2 g$ for 90T-22.4TO-S15-1123, while the specific pore volume decreases from 0.61 to 0.29 $cm^3 g$ for the same samples. On the other hand, on increasing the calcination temperature from 873 to 1273 K, the specific surface area and pore volume of the support decrease from 502 to 202 $m^2 g$ and from 0.65 to 0.31 $cm^3 g$, respectively. Figure S2 shows the nitrogen adsorption–desorption isotherm of the representative sample 15T-22.4TO-S15-1123. This sample exhibits a typical type IV isotherm, with a sharp capillary condensation step and a broad H1-type hysteresis loop, which is indicative of a narrow pore size distribution in the mesoporous material. The sharpness of the capillary condensation at higher relative pressure indicates that nitrogen condensation occurs within the mesopores, and that the sample possesses better mesostructure ordering and the pores are highly uniform even after impregnation with TiO_2 and TPA and high-temperature calcination (1123 K). The Barret–Joyner–Halenda (BJH) pore size distribution of 15T-22.4TO-S15-1123 is shown in the inset of Figure S2. The sample is seen to possess a narrow pore size distribution even after the modification. These results are in good agreement with data obtained from XRD measurements on the same sample. The surface areas of the

modified MCM-41 and MCM-48 are larger than those of the modified SBA-15 samples, although the pore diameters of the former are significantly decreased after the modification. However, the specific pore volume and the pore diameter of 15T-22.4TO-S15-1123 are larger than those of 15T-22.4TO-M41-1123 and 15T-22.4TO-M48-1123. This might be attributed to either the difference in the pore diameters of the supports or blocking of the mesoporous channels of MCM-41 and MCM-48 by the TPA or TiO_2 nanoparticles because of their smaller pore diameters as compared with the SBA-15 support. It should also be mentioned that pristine 15T-22.4TO-1123 exhibits a surface area of just $3\,m^2\,g$, which is significantly lower than those of the modified SBA-15, MCM-41, and MCM-48. This might be due to sintering of the titania support, which triggers the formation of larger particles of low acidity due to the decomposition of TPA into WO_3 and other oxides. From the above results, it is clearly apparent that supports with very high surface areas, large pore volumes, and large pore diameters are essential for the formation of TPA monolayers with small TiO_2 nanoparticles adhered to the mesochannels of the supports. As the sample 15T-22.4TO-S15-1123 showed the optimum surface area, with monolayer coverage of TPA and small TiO_2 nanoparticles on the surface, we chose this material for further characterisation.

The morphology of 15T-22.4TO-S15-1123 was determined by HRSEM and the results were compared with those obtained for pure SBA-15. The images of all of the samples show hexagonal particles organised into rope-like structures, which are further agglomerated into elongated particles. As the particle size of TiO_2 is very small, as determined by XRD, nanoparticles were not detected by SEM. However, the morphology of the parent silica support was found to be largely retained, even after the modification (Figure S3). TEM measurements were carried out in order to study the topology of the parent SBA-15 and of 15T-22.4TO-S15-1123. TEM images of pure SBA-15 and of 15T-22.4TO-S15-1123 are shown in Figure 2a and b, respectively. Both of these samples clearly exhibit highly ordered mesoporous networks with a linear array of mesopores and walls, which is characteristic of well-ordered mesoporous silica SBA-15. Further, it was found that the hexagonally arranged mesopores of SBA-15 were retained and that the TPA/TiO_2 nanoparticles were uniformly dispersed within the pores. The crystallite size of the TiO_2 nanoparticles in 15T-22.4TO-S15-1123 calculated from the TEM data was 4.5–5.5 nm, which is in good agreement with the size estimated from the XRD data using the Scherer equation.

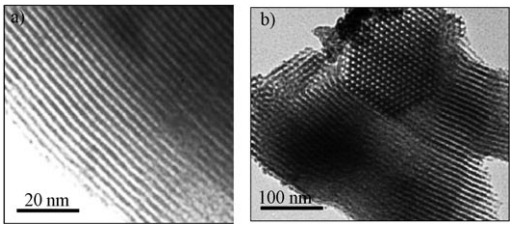

Figure 2. TEM images of a) pure SBA-15 and b) 15T-22.4TO-S15-1123.

UV/Vis diffuse reflectance spectra of 22.4TO-S15-1123 and 15T-22.4TO-S15-1123 are shown in Figure S4. 22.4TO-S15-1123 shows a sharp peak at 212.9 nm, which originates from the intense ligand-to-metal charge transfer. This can be attributed to the formation of isolated Ti ions, which mostly occupy the tetrahedral coordination sites. However, a small broad peak centred at around 320 nm is also observed for the same sample, which may be attributed to the formation of some small-sized anatase nanoparticles. On the other hand, the TPA-modified sample, 15T-22.4TO-S15-1123, shows a broad band centred at around 263.5 nm, which is coincident with the TiO_2 band. This can be assigned to the oxygen–metal charge-transfer band of the tungstophosphate anion $[PW_{12}O_{40}]^{3-}$.

FT-IR spectra of the T-TO-S15 nanocomposites prepared with different loadings of TPA, as well as of pure TPA and the pristine SBA-15 support, are shown in Figure S5. Pure TPA shows characteristic peaks at $\tilde{\nu}=1079$ (P–O), 983 (W=O_t), 893 (W-O_c-W), and 810 cm^{-1} (W-O_e-W), which are quite similar to those reported for the acid $H_3PW_{12}O_{40}$,[51] whereas pure silica exhibits IR bands at $\tilde{\nu}=1100$ and 806 cm^{-1} and a weak shoulder band at 974 cm^{-1}, which may be attributed to different forms of surface silanol groups. The TiO_2 (anatase and rutile) support absorbs below $\tilde{\nu}=$ 1100 cm^{-1}. The samples with different loadings of TPA show two sharp bands due to this additive at around $\tilde{\nu}=983$ and 888 cm^{-1}, while bands at around $\tilde{\nu}=1079$ and 810 cm^{-1} are overlapped with the strong bands of SiO_2. The sample with the highest TPA loading, that is, 90T-22.4TO-S15-1123, shows the characteristic peaks of TPA as well as a further peak at $\tilde{\nu}=983$ cm^{-1} (W=O_t). This may be attributed to the formation of WO_3 crystallites, revealing that the TPA molecules are decomposed into WO_3 when the loading of TPA is increased to 90 wt %, which is in good agreement with what was found from the corresponding XRD pattern. It must also be noted that the intensity of the peaks corresponding to TPA for the modified SBA-15 nanocomposites is much lower than in the case of pure TPA. This may be attributed to masking of the TPA bands by wide bands of support; the interaction between the Keggin anions is weakened by an increase in the distance between them.

Figure S6 shows the ^{31}P CP-MAS NMR spectrum of 15T-22.4TO-S15-1123. The sample exhibits a sharp peak centred at $\delta=-12.19$ ppm, which can be assigned to $(\equiv Ti-OH_2)^{n+}[H_{3-n}W_{12}PO_{40}]^{n-3}$ species formed by linking of the Keggin units to the TiO_2 support.[52] Water is eliminated upon heating, leading to a direct linkage between the polyanion (which probably retains a structure similar to that of the Keggin ion) and the support. The ^{31}P NMR peak of 15T-22.4TO-S15-1123 is seen to be broad. The broadening and low-field shift of the ^{31}P NMR peak are mainly due to the thermal treatment, and similar results have previously been reported by several researchers for TPA loaded onto non-porous oxide supports.[53–55] This result further indicates that the P resides geometrically at the centre of the Keggin

anion, that is, far away from the protons, and that the Keggin anion remains intact, albeit with some local distortions. ^{29}Si MAS NMR spectra of 15T-22.4TO-S15-1123 and 22.4TO-S15-1123 are shown in Figure S5b and c, respectively. The sample 22.4TO-S15-1123 shows two peaks centred at $\delta = -100$ and -110 ppm, which may be attributed to Si-$(OSi)_3(OH)$ and $Si(OSi)_4$ components, respectively,[56] whereas 15T-22.4TO-S15-1123 shows only one peak centred at around $\delta = -110$ ppm. It is interesting to note that the ^{29}Si NMR signal at around $\delta = -110$ ppm is significantly broadened upon loading with TPA, which may be attributed to the large variation in the Ti-O-Si angle.[57] A cross-polarisation technique was used because of the low concentration of P in the catalyst system since TPA and TiO_2 were embedded inside the mesoporous channels.

Figure 3 shows FT-IR spectra of adsorbed pyridine in 15T-22.4TO-S15-1123. The ratios of Brønsted (B) to Lewis (L) acid sites (B/L) calculated from the IR absorbance intensities in FT-IR spectra of adsorbed pyridine in 22.4TO-S15-1123 with different TPA and TiO_2 loadings and in 15T-22.4TO-S15-1123 calcined at different temperatures are given in Table 1, while the corresponding B/L ratios for different catalysts are compared with their catalytic activities in Table 2. FT-IR spectra of pyridine adsorbed on all of the catalysts were recorded in the range 100–400 °C under a flow of N_2. At 100 °C, the important pyridine ring modes are seen at approximately $\tilde{\nu} = 1609$, 1540, 1489, and 1445 cm^{-1}.

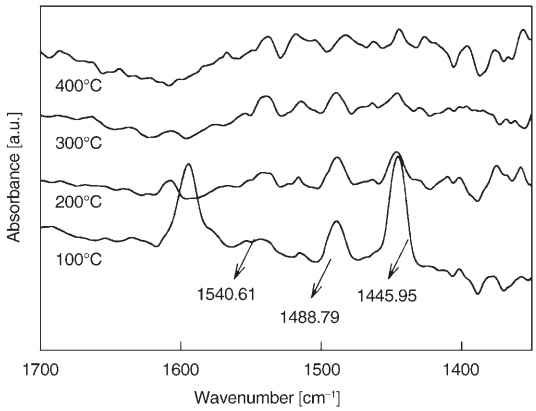

Figure 3. FT-IR spectra of pyridine adsorbed within 15T-22.4TO-S15-1123.

As can be seen in Figure 3, pyridine molecules bonded to Lewis acid sites give rise to a peak at $\tilde{\nu} = 1445$ cm^{-1}, whereas those that interact with Brønsted acid sites (pyridinium ions) display absorbances at 1540 and 1640 cm^{-1}. The band at 1489 cm^{-1} is a combined band originating from pyridine bonded to both Brønsted and Lewis acid sites. The relative intensities of the absorbances at $\tilde{\nu} = 1540$ and 1445 cm^{-1} attributable to the Brønsted (B) and Lewis (L) acid sites were used to calculate the B/L ratio.[58] It was found that the B/L ratio increases with increasing TPA loading up to 15 wt%, but then decreases when the loading of TPA is increased further. This suggests that 15T-22.4TO-S15-1123 possesses the highest acidity among the samples prepared in this study. This may be due to the monolayer coverage of TPA and TiO_2, which are uniformly dispersed inside the mesochannels of the SBA-15 support. It is also worthy of note that the B/L ratio decreases with increasing TPA loading from 15 to 90 wt%. This decrease in B/L ratio may also be attributed to decomposition of the TPA because a higher TPA loading exceeds monolayer coverage on the surface of the support. The Brønsted acidity increases with increasing TPA loading from 0 to 15 wt% and then decreases thereafter, whereas only Lewis acidity is observed for samples with very low TPA loading. The decrease in acidity above 15 wt% may be due to the formation of crystalline WO_3, which prevents the pyridine from accessing the active sites.

Besides the TPA loading, the nature of the acidity in 15T-22.4TO-S15-1123 is significantly affected by the calcination temperature. The Brønsted acidity increases with increasing calcination temperature up to 1123 K (due to monolayer coverage), but then the B/L ratio decreases on further increasing the calcination temperature beyond 1123 K (Table 1). Following calcination at a low temperature (823 K), the catalyst 15T-22.4TO-S15-823 exhibits mainly Lewis acidity and very low Brønsted acidity. This is mainly due to the fact that the calcination process enhances dehy-

Table 2. Effect of the textural parameters on the hydroamination of aniline by EA over various supports.

Sample	SA [m^2g^{-1}]	PV [cm^3g^{-1}]	PD [Å]	TA [$mmol\,g^{-1}$]	B(L)	B/L	TOF [s^{-1}]$\times10^{-2}$[a]	RC$\times10^{-5}$ [s^{-1}]	Conv. [%]
SBA-15	929	1.36	73.3	–	–	–	–	–	–
MCM-41	1155	0.88	30.5	–	–	–	–	–	–
MCM-48	1096	0.71	26.1	–	–	–	–	–	–
22.4TO-S15-1123	403	0.67	71.8	0.28	0.053 (0.059)	0.90	–	3.81	24
22.4TO-M41-1123	510	0.34	27.5	0.22	0.037 (0.168)	0.22	–	1.62	11
22.4TO-M48-1123	587	0.60	24.2	0.08	0.019 (0.21)	0.09	–	1.14	7.9
15T-22.4TO-S15-1123	353	0.55	68.7	0.38	0.097 (0.069)	1.40	11.9	12.05	58
15T-22.4TO-M41-1123	426	0.25	16.5	0.29	0.047 (0.247)	0.19	3.2	2.41	15.9
15T-22.4TO-M48-1123	488	0.20	15.9	0.20	0.047 (0.336)	0.14	2.2	1.57	10.7
3.36TPA-S15	340	0.59	69.9	0.27	0.028 (0.034)	0.83	5.7	4.56	28
15TPA-TO	3	–	–	0.02	0.018 (0.019)	0.97	2.0	1.43	9.8

[a] TOF is calculated by considering three protons per Keggin unit ($mol\,mol^{-1}$ H^+s^{-1}). Conditions: aniline (1.45 g, 0.016 mol) + ethyl acrylate (EA) (1.55 g, 0.016 mol), aniline/EA (mole ratio) = 1, catalyst = 0.3 g, T = 383 K, t = 2 h; SA = surface area; PV = pore volume; PD = pore diameter; TA = total acidity; B/L = ratio of Brønsted and Lewis acid sites; TOF = turnover frequency; RC = rate constant; Conv. = conversion.

droxylation of the support, which results in much better crystallisation. In this process, the interaction between the TPA and the support is partially weakened, giving rise to free H^+ ions that act as Brønsted acid sites. Moreover, the effect of the TiO_2 loading on the acidity of the catalytic system has been studied. The Brønsted acidity was found to increase on increasing the TiO_2 loading from 10 to 22.4 wt% and then decreased on further increasing the TiO_2 loading to 90 wt%. It was thus concluded that the threshold value for monolayer dispersion of TiO_2 over SBA-15 was 22.4%, and that a TPA loading of 15 wt%, a TiO_2 loading of 22.4 wt%, and a calcination temperature of 1123 K represented the optimum conditions for obtaining nanocomposites with the highest acidity.

XPS analysis has been used to investigate the interaction between the guest (TiO_2) and the host (SBA-15). It was found that TiO_2 is most likely to interact with SBA-15 through hydrogen bonds involving the Si-OH groups of the SBA-15 and the titanium atoms of TiO_2. As a result of this interaction, free hydrogen is available on the SBA-15 support at monolayer coverage. Below a loading of 22.4 wt% TiO_2, this interaction is less prominent due to the low TiO_2 content, whereas above this loading it is suppressed by multilayer formation on the mesoporous support. Thus, the Brønsted acidity of the catalyst increases with both TPA loading and calcination temperature up to a monolayer of TPA on TiO_2. It has been reported that pure TPA shows mainly Brønsted-type acidity, while the titanium oxyhydroxide support is known to be amphoteric in character. Interaction between the titanium oxyhydroxide and TPA neutralises the Brønsted acid sites of TPA with the formation of $(Ti(OH_2)^{n+})(H_{3-n}W_{12}O_{40})$ species. The higher Lewis acidity at lower calcination temperature shows that the Lewis acidity mainly originates from the support itself. At higher calcination temperature, dehydration/dehydroxylation occurs and the interaction between the TPA and the support is enhanced. This helps the anchoring of the TPA onto the titania through Ti–O–W bonds, which generates the Brønsted acid sites. The formation of such Brønsted acid sites is also observed in titania-supported isopolytungstate catalysts.[59]

Figure 4A shows a comparison of the O 1s X-ray photoelectron spectra of 15T-22.4TO-S15-1123 and 22.4TO-S15-1123. The spectra can be deconvoluted into three sharp peaks, which are centred at 528, 530.6, and 531.8 eV. It should be noted that the intensity of the peak at 531.8 eV is much higher than that of the peak at 528 eV. The lowest-energy contribution is attributed to the coordination of the Ti atoms by the hydroxyl groups of the support, whereas the highest-energy contribution is attributed to the oxygen in the Si-O-Ti linkages in the nanocomposites. In accordance with the literature on TiO_2 anatase nanoparticles on silica, the peak at 530.6 eV is attributed to the oxygen in titania, which corresponds to Ti–O–Ti bonds.[60] A small shift in the binding energy for the sample was observed after the loading with TPA. The binding energy of the oxygen in the titania is slightly shifted to a higher value relative to that of oxygen in pure titania. This may be due to the greater elec-

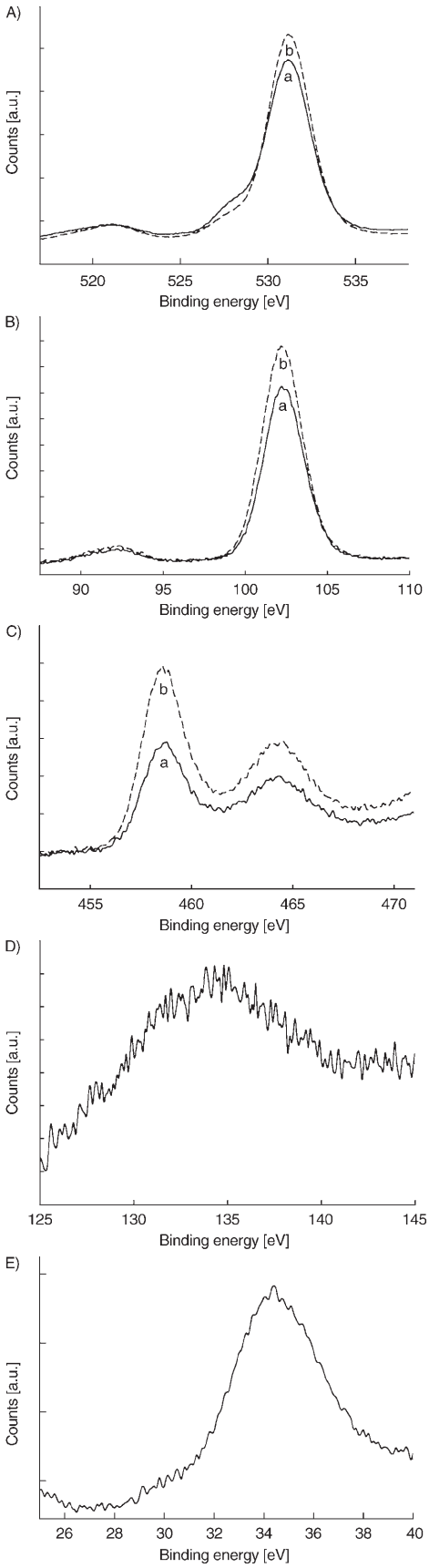

Figure 4. X-ray photoelectron spectra of A) O 1s, B) Si 2p, C) Ti, D) P 2p, and E) W $4f_{7/2}$ of samples calcined at 1123 K: a) 22.4TO-S15-1123 and b) 15T-22.4TO-S15-1123.

tronegativity of Si compared to that of Ti. This shift in the binding energy also proves the formation of a titania coating layer on the surface of the silica particles involving Ti–O–Si bonds. Similar conclusions were reached by inspection of the Si 2p X-ray photoelectron spectra of these samples (Figure 4B). These results also support the interaction of a titania layer, and the presence of an anatase titania phase on the silica supports. Moreover, no significant change in the full width at half maximum (FWHM) of the Si 2p spectra of the samples was observed, suggesting that the structure of the silica is not affected by the impregnation process.

Figure 4C shows a comparison of the Ti 2p X-ray photoelectron spectra of 15T-22.4TO-S15-1123 and 22.4TO-S15-1123. The binding energies of the Ti $2p_{3/2}$ and Ti $2p_{1/2}$ peaks, which are located at about 458.7 and 464.3 eV for both samples, are given in Table S1. The binding energies of the Ti $2p_{3/2}$ peak and Ti $2p_{1/2}$ peaks are shifted to higher values relative to those of pure anatase titania (Figure 4C). This also provides further evidence for the formation of Ti–O–Si bonds. The P 2p phosphorus signal at 134.4 eV, which is very weak due to the presence of only a small quantity in the sample, may be attributed to a compound that contains P–O bonding (Figure 4D). However, high FWHM values are observed as a result of peak broadening, which might be due to differential charging of the sample caused by the mesoporous silica support. The two peaks of the spin-orbit split doublet of tungsten, W $4f_{7/2}$ and W $4f_{5/2}$ with a FWHM of 4.5 eV, are located at 35.2 and 36.7 eV, respectively (Figure 4E). The observed binding energy of W ($4f_{7/2}$) is 35.6 eV, a characteristic of W^{6+}, indicating that the sample contains W–O bonding.[61]

FT-Raman spectra of 15T-22.4TO-S15-1123 and 22.4TO-S15-1123 are shown in Figure 5, and the observed Raman frequencies are listed in Table S2. Titania can exist in three crystalline modifications, namely rutile (tetragonal), anatase (tetragonal), and brookite (orthorhombic). Each octahedron in anatase is connected to two edge-sharing octahedra and eight corner-sharing octahedra, compared with rutile with four edge-sharing octahedra and four corner-sharing octahedra. Anatase has a space group D_{4h} ($I_4$1/amd) containing two formula units per primitive unit cell. From group analysis, there are six Raman-active modes ($A_{1g}+2B_{1g}+3E_g$), which were identified as 144 cm^{-1} (E_g), 197 cm^{-1} (E_g), 399 cm^{-1} (B_{1g}), 513 cm^{-1} (A_{1g}), 519 cm^{-1} (B_{1g}), and 639 cm^{-1} (E_g) (Figure S6). Rutile has two molecules in the unit cell, and the space group D_{4h} ($P_4$2/mnm), implying a total of four Raman-active modes: A_{1g}, B_{1g}, B_{2g}, and E_g, which were detected at 143 cm^{-1} (B_{1g}), 447 cm^{-1} (E_g), 612 cm^{-1} (A_{1g}), and 826 cm^{-1} (B_{2g}).

It was observed that 22.4TO-S15-1123 contained anatase as well as rutile-type components, whereas the sample 15T-22.4TO-S15-1123 exhibited only anatase-type titania, suggesting that the addition of TPA helped the rutile-to-anatase phase transition, which is required for the catalysis. An additional Raman peak at 276 cm^{-1} was observed for both of these samples, which may be attributed to Ti–O bonds. Similar peaks are also observed for sodium titanate with a layered structure. A broad weak band at 830.2 cm^{-1} may be attributed to covalent Ti–O–H bonds, which originate from interaction between the silica support and the titania, whereas the peak at 278.9 cm^{-1} may be attributed to the formation of nanocrystalline titania. Peaks corresponding to TPA were also observed for the nanocomposites. Bands at around 1009 and 992 cm^{-1}, and a weak peak at around 905 cm^{-1}, could be assigned to pure TPA.[62] These bands broadened and shifted towards higher wavenumber upon the addition of TPA. This may be ascribed to the formation of Keggin anionic species through linking of the Keggin units to the titania support.

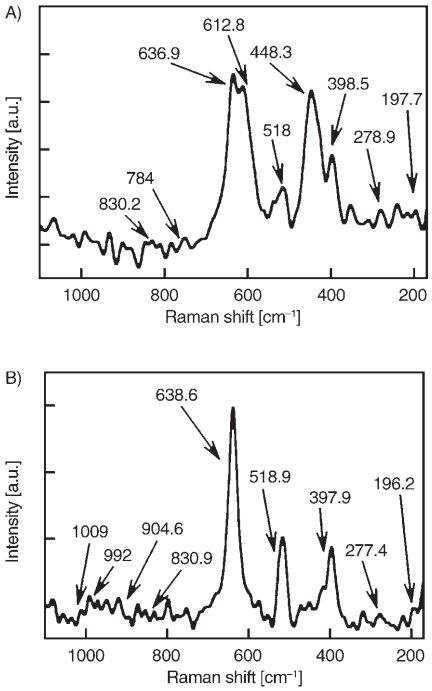

Figure 5. FT-Raman spectra of A) 22.4TO-S15-1123 and B) 15T-22.4TO-S15-1123.

The NH_3 temperature-programmed desorption (TPD) technique usually enables determination of the strength of the acid sites present on a catalyst surface, as well as the total acidity. Generally, the temperature at which NH_3 is desorbed is related to the strength of the acidic sites. A higher temperature for NH_3 desorption indicates more strongly acidic sites in the samples. The NH_3-TPD profiles for 15T-22.4TO-S15-1123 and 22.4TO-S15-1123 are shown in Figure 6. Both of these catalysts show a broad TPD profile, revealing a wide distribution in the strengths of the surface acid sites. According to the areas under the peaks, 15T-22.4TO-S15-1123 shows higher acidity than 22.4TO-S15-1123. Total acidities in terms of the amounts of NH_3 in mmol g^{-1} for the catalysts with different loadings of TPA and TiO_2 and calcined at different temperatures are presented in Table 1. It is evident from the data in Table 1 that the total acidity of the catalyst increases with increasing TPA loading from 0 to 15 wt% and then reaches a maximum. A further increase in the TPA loading beyond 15 wt% results

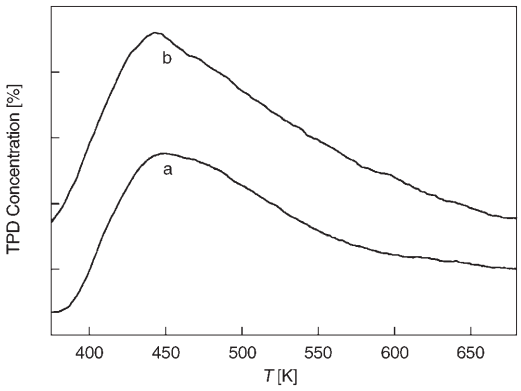

Figure 6. TPD of ammonia of a) 22.4TO-S15-1123 and b) 15T-22.4TO-S15-1123.

in a decrease in the total acidity of the samples, which incidentally have lower surface areas. These results indicate that TPA and TiO_2 are uniformly dispersed over the SBA-15. The calcination temperature was also found to affect the total acidity of the samples. The amount of NH_3 desorbed was found to increase with increasing calcination temperature and reached a maximum for the material calcined at 1123 K. On further increasing the calcination temperature from 1123 to 1273 K, the total acidity decreased drastically from 0.38 to 0.31 mmol g^{-1}, which was mainly due to the decomposition of TPA into WO_3 crystallites. Similarly, when the loading of TiO_2 was increased from 0 to 22.4 wt%, the catalyst showed an increase in the total acidity, which was also reflected in the catalytic activity obtained (vide infra). Overall, it may be concluded that at low TPA loadings the Keggin-like unit of the heteropoly acid retains its structure and acidity, whereas at higher loadings (above 15 wt% TPA) it partly decomposes to its oxides. The highest acidity seen for 15T-22.4TO-S15-1123 corresponds to monolayer coverage with TPA, where the Keggin-like structure is intact, as supported by FT-IR, Raman, XRD, XPS, and UV/Vis spectroscopic techniques. From the above results, we can conclude that 15T-22.4TO-S15-1123 is superior to all of the other catalysts prepared under different conditions. Thus, this catalyst was selected for use in studies of catalytic performance.

Catalytic activity

Hydroamination reaction: The reaction mechanism for the hydroamination of ethyl acrylate (EA) with aniline is shown in Scheme 1.

To test the effectiveness of the present catalytic system, the hydroamination of EA with aniline was performed under liquid-phase reaction conditions at 383 K. The reaction conditions and the results obtained are presented in Tables 1 and 2. A control experiment was carried out under the same conditions without addition of any catalyst. As expected, only 2% conversion was achieved without the catalyst. Among the catalysts studied, 15T-22.4TO-S15-1123

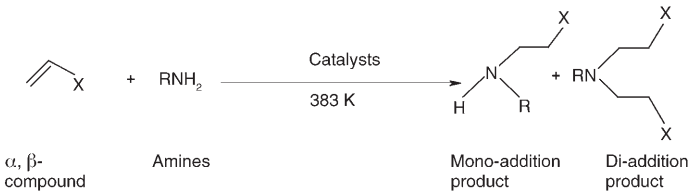

Scheme 1. Schematic representation of the hydroamination reaction.

showed the highest activity, giving a yield of almost 90% of the anti-Markovnikov adduct, that is, *N*-[2-(ethoxycarbonyl)-ethyl]aniline (mono-addition product). Neither the Markovnikov adduct *N*-[1-(ethoxycarbonyl)ethyl]aniline nor the double-addition product *N*,*N*-bis[2-(ethoxycarbonyl)ethyl]aniline were formed. The recyclability of the catalyst 15T-22.4TO-S15-1123 was studied. It was found that a second reuse gave the product in similar yield and purity as a first run with recycled catalyst (1st cycle 57.1%; 2nd cycle 56.4%). This confirmed that the catalyst was highly stable and could be regenerated.

Mannich reaction: Mannich reactions of aldehydes, ketones, and amines were carried out over 15T-22.4TO-S15-1123 at both room temperature and 333 K. The results (yield of Mannich product) are presented in Table 3. Under the slightly acidic conditions, an iminium salt was formed, which could be considered as a Mannich intermediate (Scheme 2). This was followed by electrophilic attack by the iminium salt on the enol-form of the active methylene compound. The free base could be obtained by treating the solution with an alkali at the end of the reaction.

Table 3. Effect of reaction temperature and the reactants on the catalytic activity of 15T-22.4TO-S15-1123 in the Mannich reaction.[a]

Entry	Aldehyde	Amine	Ketone	T [K]	t [h]	Yield [%]
1[b]	**1a**	**1b**	**1c**	RT	12	0
				333	6	0
2	**1a**	**1b**	**1c**	RT	12	55[c]
				333	6	49
3	**2a**	**1b**	**1c**	RT	12	98.7[d]
				333	6	99.8
4	**1a**	**2b**	**1c**	RT	12	0
				333	6	0
5	**1a**	**3b**	**1c**	RT	12	75[e]
				333	6	72
6	**1a**	**1b**	**2c**	RT	12	0
				333	6	0
	recyclability of the catalyst for the Mannich reaction					
7	**2a**	**1b**	**1c**	333	6	98.2
8	**2a**	**1b**	**1c**	333	6	97.6

[a] Reaction conditions: aldehyde/amine/ketone 1:1:1 (mole ratio), catalyst: 15T-22.4TO-S15-1123 (0.3 g, 10 wt.% of total reaction mixture); **1a** = benzaldehyde, **1b** = aniline, **1c** = acetophenone, **2a** = 3-chlorobenzaldehyde, **2b** = 2,4-xylidene, **3b** = 4-bromoaniline, **2c** = 2-hydroxyacetophenone. [b] Without catalyst. [c] 3-(*N*-Phenylamino)-1,3-diphenyl-1-acetone. [d] 3-(*N*-Phenylamino)-3-(3-chlorophenyl)-1-phenylacetone. [e] 3-(*N*-4-Bromophenylamino)-1,3-diphenyl-1-acetone.

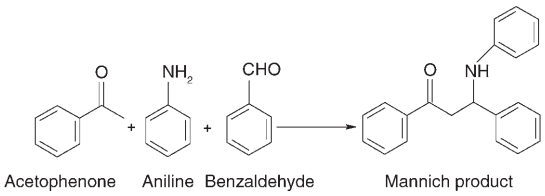

Scheme 2. Schematic representation of the Mannich reaction.[67]

The reaction of 3-chlorobenzaldehyde with aniline and acetophenone gave the product in 98.7% yield (Table 3, entry 5), whereas with 4-bromoaniline a yield of 75% was produced over a period of 12 h (Table 3, entry 9). On the other hand, only 55% yield was obtained when benzaldehyde was used instead of halo-substituted benzaldehydes (Table 3, entry 3). No Mannich base was observed when 2,4-xylidene and *o*-hydroxy acetophenone were used. This may have been due to steric hindrance (Table 3, entries 4 and 6).

Claisen rearrangement reaction: The Claisen rearrangement of allyl phenyl ether (APE) was carried out over 15T-22.4TO-S15-1123 and the results were compared with those achieved with 22.4TO-S15-1123 and without a catalyst. The catalyst 15T-22.4TO-S15-1123 was found to be highly active, showing almost 100% conversion of APE and high selectivity in the formation of 2,3-dihydro-2-methylbenzofuran. The results of the experiments are presented in Table 4. A plausible mechanism for the production of allylphenol and its subsequent conversion to the ring compound by the Claisen rearrangement is presented in Scheme 3. The allyl group migrates from the oxygen atom of the ether group to a carbon atom of the aromatic ring. The migrant allyl group goes preferentially to either the *ortho* position or to the *para* position if both *ortho* positions are blocked. Rearrangement to the *ortho* position is a concerted process involving a cyclic six-membered transition state, in which rupture of the oxygen–allyl bond is synchronous with the formation of a carbon–carbon bond at the *ortho* position. Thus, the reaction proceeds via a cyclohexadiene intermediate, which undergoes prototropic rearrangement to the more stable aromatic compound, phenol (A). The steps are catalysed by the acid sites. Initially, the acid site protonates the oxygen of the ether group, and this is followed by intramolecular rearrangement of the protonated (adsorbed) species into the *o*-allylphenol (A). The allylphenol is then protonated at the allylic double bond to produce the secondary carbenium ion, which reacts intramolecularly once more with the phenolic oxygen to produce the benzofuran (B). Various solvents were tested for their suitability for this reaction. Tetrachloroethylene proved to be the best solvent, giving *o*-allylphenol and 2,3-dihydro-2-methylbenzofuran with a product selectivity of 39:61. As shown in Table 3, 15T-22.4TO-S15-1123 showed almost five-fold higher activity than 22.4TO-S15-1123.

Table 4. Claisen rearrangement of an allyl phenyl ether at 383 K.[a]

Entry	Catalyst	APE conversion [%]	Selectivity [%]	
			o-allyl-phenol	2,3-dihydro-2-methylbenzofuran
1	blank	0	0	0
2	22.4TO-S15-1123	15	100	0
3	15T-22.4TO-S15-1123	81	39	61
		recyclability		
1	1st cycle	79	41	59
2	2nd cycle	78	42	58

[a] Reaction conditions: allyl phenyl ether/catalyst (molar ratio) = 1:0.1, APE (3 g), solvent: tetrachloroethylene (5 g), $T = 383$ K, $t = 12$ h.

The catalyst proved to be readily recyclable after separating it from the reaction mixture. Indeed, 15T-22.4TO-S15-1123 was recycled two times, and reusing the same catalyst for a second run gave the products in similar yield and purity as in a first run with recycled material (Tables 3 and 4). This shows that the catalyst was highly stable and could be regenerated several times under the specified reaction conditions.

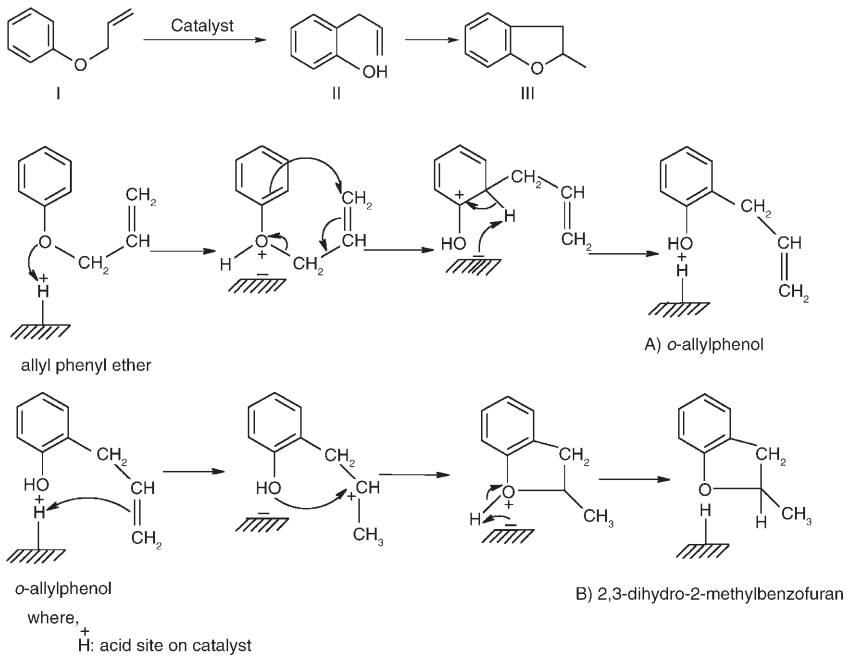

Scheme 3. Schematic representation of the Claisen rearrangement reaction.[68,69]

Conclusion

We have demonstrated for the first time the preparation of SBA-15/TiO_2 mesoporous nanocomposites with different loadings of TPA nanocrystals through a simple and effective vacuum impregnation method. The catalysts have been unambiguously characterised by many sophisticated instrumental techniques, such as XRD, N_2 adsorption, HRSEM, TEM, FT-IR, UV/Vis, NMR, FT-Raman, XPS, TPD of NH_3, and FT-IR of adsorbed pyridine. It has been observed that the acidity and the textural parameters of the nanocomposites can be controlled by simply changing the loadings of TPA and TiO_2 or the calcination temperature. We conclude that the amounts of TPA and TiO_2 loaded on the surface of the mesoporous silica supports is one of the main critical factors that controls the acidity of the catalysts. Moreover, the activity of these catalysts in hydroamination, Mannich, and Claisen rearrangement reactions has been extensively investigated. The effects of various parameters, such as the reaction temperature and duration, on the conversion and product selectivity have also been studied in detail. A nanocomposite material with 15 wt% TPA and 22.4 wt% TiO_2 calcined at 1123 K was found to be the best catalyst, showing higher activity in the aforementioned acid-catalysed organic transformations than pristine TPA, TiO_2-loaded SBA-15, or other nanocomposites made from MCM-41 and MCM-48. It has been found that the performances of these nanocomposite catalysts are strongly influenced by the loadings of TPA and TiO_2 and by the calcination temperatures, and, most importantly, by the nature and the characteristics of the nanocomposites. Moreover, the promising results achieved with these nanocomposite catalysts in promoting various organic transformations suggest that they are highly acidic and attractive for acid-catalysed reactions and might thus pave the way for ecologically and environmentally friendly processes to supersede the use of conventional homogeneous TPA catalysts.

Experimental Section

Materials: Hexadecyltrimethylammonium bromide (CTABr) (Aldrich; >99%), tetraethyl orthosilicate (Aldrich; >99%), a triblock copolymer of ethylene oxide (EO) and propylene oxide (PO), $EO_{20}PO_{70}EO_{20}$ (P123) (Aldrich; $M_{avg}=5800$), titanium chloride ($TiCl_4$) (Merck; 99.5%), and 12-tungstophosphoric acid (TPA) (Merck; >99.9%) were used without further purification for the synthesis of the mesoporous materials. Allyl phenyl ether (99%), benzaldehyde (99%), and acetophenone (99%) were procured from Aldrich. All of the aliphatic and aromatic amines, as well as toluene, were obtained from S.D. Fine Chemicals, Mumbai. Ethyl acrylate was purchased from Lancaster Synthesis, UK. All substrate chemicals were used as received. Toluene used in the reaction was distilled over sodium wire before use. All catalysts used in the reactions were in powder form and were activated prior to their deployment.

Synthesis of mesoporous silica MCM-41: Pure siliceous MCM-41 material was prepared as described in the literature.[63] The gel composition used for its preparation was as follows 10 SiO_2: 5.4 CTABr: 4.25 Na_2O: 1.3 H_2SO_4: 480 H_2O. Si-MCM-41 was prepared as follows: CTABr (32 g) was dissolved in water (115 g) and the solution was stirred for 30 min at room temperature. Sodium silicate solution (37.4 g) in water (23.4 g) was then added dropwise to the surfactant solution under vigorous stirring, and stirring was continued for a further 30 min. Subsequently, a solution of H_2SO_4 (2.4 g) in water (10 g) was added to the above mixture and stirring was continued for a further 30 min. The resulting gel was transferred to a polypropylene bottle and kept in an oven at 373 K for 24 h. After cooling to room temperature, the solid obtained was collected by filtration, washed with distilled water, and dried in an oven at 373 K for 6 h. Finally, the material was calcined in a muffle furnace at 813 K for 10 h.

Synthesis of mesoporous silica MCM-48: MCM-48 was synthesised according to the procedure described in the literature.[64] The molar composition of the gel was 1 TEOS: 0.25 Na_2O: 0.65 CTABr: 0.62 H_2O. CTABr (31.2 g) was dissolved in deionised water (93.6 g) and the solution was stirred at 318 K for 40 min. TEOS (30 g) was then added, followed by 1 M sodium hydroxide solution (69 g), and the mixture was stirred at room temperature for a further 1 h. The resulting gel was then transferred to a polypropylene bottle and kept in an oven at 373 K for 72 h under static conditions. After cooling to room temperature, the solid formed was collected by filtration, washed with ethanol and with distilled water, and dried in air in an oven at 373 K for 6 h. Finally, the material was calcined in a muffle furnace at 813 K for 10 h.

Synthesis of mesoporous silica SBA-15: SBA-15 was synthesised with a gel composition of 0.0007 P123: 0.041 TEOS: 0.24 HCl: 6.67 H_2O according to the literature procedure[65] as follows: P123 (4 g) was dispersed in water (30 g) and the suspension was stirred for 4 h. 2 M HCl solution (120 g) was then added and the mixture was stirred for 2 h. A homogeneous solution was obtained, to which TEOS (8.54 g) was added with stirring. The resulting gel was aged at 313 K for 24 h and finally heated to 373 K for 48 h. Following the synthesis, the solid was collected by filtration, washed with distilled water, and dried in air in an oven at 373 K for 5 h. Finally, it was calcined at 813 K to remove the triblock copolymer.

Mesoporous silica embedded TiO_2-supported HPA: Mesoporous silica SBA-15 (2 g) was first wet-impregnated with an aqueous solution of titanium tetrachloride in a rotary evaporator under a vacuum of 10^{-7} Torr attained by means of a turbo pump. The titanium tetrachloride solution was prepared in deionised water using high-speed stirring in an ice-water bath under air-tight conditions. An excess of this solution (10, 22.4, 30, 50, and 70 wt%) was introduced and was kept in contact with the silica for 6 h under vacuum. The volatiles were then stripped off and the solid was dried at 100°C in air. A similar procedure was subsequently used for the wet-impregnation of TPA (10, 15, 30, 50, 70, and 90 wt%) on an optimised 22.4 wt% TiO_2 loaded on SBA-15. In addition, samples with 15 wt% TPA on different TiO_2-loaded SBA-15 substrates were also prepared. All of the catalysts were dried overnight at 373 K in air in an oven and were further calcined at 1123 K. The nanocomposites were calcined at different temperatures. The samples were named as xT-yTO-S15-z, where x, y, T, TO, S15, and z denote the wt% of TPA, the wt% of titania, TPA, TiO_2, SBA-15, and the calcination temperature, respectively. For comparison purposes, catalysts composed of 15 wt% TPA loaded on 22.4 wt% TiO_2 on MCM-41 (15T-22.4TO-M41-1123), 15 wt% TPA loaded on 22.4 wt% TiO_2 on MCM-48 (15T-22.4TO-M48-1123), and neat 15 wt% TPA loaded on pure TiO_2 (15T-TO-1123) were prepared by a similar procedure and all were calcined at 1123 K. To study the roles of titania and TPA in the composite materials, samples with 22.4 wt% TiO_2 loaded on SBA-15 (22.4TO-S15-1123) and 3.36 wt% TPA loaded on SBA-15 (3.36T-S15-1123) were also prepared and calcined at 1123 K.

Characterisation of the catalysts: The Ti, W, and P contents in the resulting solids were determined by inductively coupled plasma-optical emission spectroscopy (ICP-OES) and X-ray fluorescence spectrophotometry using a Rigaku 3070E model sequential X-ray photoelectron spectrometer (XRF) with an Rh target. XRD patterns were determined with a Bruker instrument equipped with a general area detector diffraction system (GADDS) using $Cu_{K\alpha}$ radiation at a step size of 0.01°, the generator operating at 40 kV and 40 mA. The tetragonal crystallite size in the various samples was estimated from the integral line width using the Scherer relationship[66] $D_{hkl}=0.9\lambda/B_{hkl}\cos\theta$, where B_{hkl} is the effective line width of the X-ray reflection. BET surface area data, pore volumes, and pore size distributions of the samples were determined from N_2 ad-

sorption isotherms measured with an Omnisorb 100 CX system (Coulter, USA) using N_2 gas as the adsorbent at liquid N_2 temperature.

The morphology and the topology of the nanocomposite materials were observed using a JEOL JSM-5200 scanning electron microscope (SEM) with a resolution of 5.5 nm and a JEOL model 1200 EX transmission electron microscope (TEM) operated at an accelerating voltage of 120 kV, respectively. The nature and the coordination of the silica support before and after modification were elucidated by ^{29}Si MAS NMR on a Bruker DRX-500 MHz spectrometer and ^1H MAS NMR on a Bruker DSX-300 MHz spectrometer. The state of the TPA in the catalyst was elucidated by ^{31}P CP-MAS NMR (Bruker DSX-300 MHz spectrometer). ^{31}P CP-MAS NMR was performed at 121.5 MHz with high-power decoupling and a Bruker 4 mm probehead. The spinning rate was 10 kHz, and the delay between two pulses was varied between 1 and 30 s to ensure complete relaxation of the ^{31}P nuclei. Chemical shifts are given relative to external 85 % H_3PO_4. DRS spectra of solid samples were recorded in the range 200–600 nm using a Shimadzu UV-2101 PC spectrophotometer fitted with a diffuse reflectance chamber with an inner surface of $BaSO_4$. A Shimadzu FTIR-8201 PC unit set to DRS mode with a measurement range of 600–1200 cm^{-1} was used to obtain FT-IR spectra of the nanocomposites. Raman spectra were obtained on a Bruker FRA106 spectrometer equipped with an Nd/YAG (neodymium/yttrium aluminium garnet) laser. Spectra were collected at room temperature in the wavelength range 0 to 4000 cm^{-1} at a spectral resolution of 5 cm^{-1}. X-ray photoelectron spectra (XPS) were recorded on a VG Microtech Multilab-ESCA 3000 spectrometer equipped with a twin anode of Al and Mg. All measurements were carried out on powder samples using $Mg_{K\alpha}$ X-ray radiation at room temperature. The base pressure in the analysis chamber was 4×10^{-10} Torr. A multichannel detection system with nine channels was employed to collect the data. The overall energy resolution of the instrument was better than 0.7 eV, as determined from the full-width at half-maximum of the $4f_{7/2}$ core level of a gold surface. The errors in the binding energy (BE) values were within ±0.1 eV. A binding energy correction was performed using the C_{1S} peak of carbon at 284.9 eV as a reference.

The overall acidity of the catalysts was estimated by temperature-programmed desorption (TPD) of NH_3 on a Micromeritics AutoChem 2910 instrument. These experiments were performed by first dehydrating a 0.1 g sample of the catalyst at 500 °C in dry air for 1 h and purging with helium for 0.5 h. The temperature was decreased to 125 °C under the flow of helium and then 0.5 mL pulses of NH_3 were supplied to the samples until no more NH_3 uptake was observed. The NH_3 was then desorbed in the He flow by increasing the temperature to 540 °C at a heating rate of 10 °C min^{-1} and measured with a TCD. The nature of the acid sites (Brønsted and Lewis) of the catalyst samples with different loadings was characterised by in situ FT-IR spectroscopy of chemisorbed pyridine; spectra were acquired in drift mode on a Shimadzu FTIR-8300 SSU-8000 instrument with 4 cm^{-1} resolution and averaged over 500 scans. These studies were performed by heating pre-calcined powder samples in situ from room temperature to 400 °C at a heating rate of 5 °C min^{-1} in a flowing stream (40 mL min^{-1}) of pure N_2. The samples were kept at 400 °C for 3 h and then cooled to 100 °C, whereupon pyridine vapour (20 μL) was introduced under N_2 flow and IR spectra were recorded at different temperatures up to 400 °C.

Experimental procedure for the determination of catalytic activity: The liquid-phase hydroamination of α,β-ethylenic compounds with amines, the Mannich reaction, and the Claisen rearrangement of an allyl phenyl ether were each performed in a 50 mL two-necked flask equipped with a nitrogen inlet for maintaining an inert atmosphere and an additional port fitted with a septum for sample withdrawal. The temperature of the reaction vessel was maintained using an oil bath. The catalysts were activated at 773 K for 4 h in air at a flow rate of 5 mL min^{-1} and then cooled to room temperature prior to their use in the reactions.

Hydroamination reaction: The hydroamination reaction was carried out under selected conditions, that is, at 383 K with an ethyl acrylate (hereafter abbreviated as EA) to aniline molar ratio of 1 and with 5 wt % (total reaction mixture) of the catalyst. The reaction mixture was magnetically stirred and heated to the required temperature under atmospheric pressure. Samples were withdrawn at regular intervals and analysed using a gas chromatograph (HP-6890) equipped with an FID detector and a capillary column. The products were also identified by GC-MS (HP-5973) analysis. Conversion was calculated based on the amine. After completion of the reaction, the reaction mixture was cooled to room temperature and filtered to remove the catalyst, and the solvent was removed by distillation. The product was separated by column chromatography using neutral alumina as the stationary phase and petroleum ether/ethyl acetate (95:5) as the eluent. The product was characterised by ^1H NMR, ^{13}C NMR, GC-MS, and FT-IR analysis, which confirmed it to be *N*-[2-(ethoxycarbonyl)ethyl]aniline. Yield: 90 %; ^1H NMR (200 MHz, $CDCl_3$): $\delta=7.21$–7.06 (m, 2H), 6.68–6.53 (m, 3H), 5.21 (s, 1H), 4.13–4.01 (m, $J=3.72$ Hz, 2H), 3.41–3.34 (t, $J=6.45$ Hz, 2H), 2.57–2.47 (q, $J=6.32$ Hz, 2H), 1.22–1.14 ppm (t, $J=7.07$ Hz, 3H); ^{13}C NMR ($CDCl_3$, 200 MHz): $\delta=172.43$ (C), 147.73 (C), 129.52 (CH), 129.34 (CH), 117.72 (CH), 113.10 (CH), 112.70 (CH), 60.64 (CH_2), 39.51 (CH_2), 34.02 (CH_2), 14.24 ppm (CH_3); FT-IR (neat): $\tilde{\nu}=3409$, 2985, 1731, 1604, 1504, 1373, 1319, 1249, 1176, 1099, 1029, 1864, 748, 694 cm^{-1}; GC-MS: *m*/*z* (%): 193 (11.83), 118 (2.55), 106 (100), 93 (2.46), 77 (11.26), 65 (6.57), 51 (7.79).

Mannich reaction: Typically, benzaldehyde (1 equiv, 1 g), aniline (1 equiv, 0.87 g), acetophenone (1 equiv, 1.13 g), and 15T-22.4TO-S15-1123 (0.3 g) were stirred at room temperature or at 333 K in a round-bottomed flask fitted with a condenser. After a certain time, the reaction mixture became viscous and solidified. At this point, the time was noted and the catalyst was separated from the reaction mixture by filtration followed by extraction with dichloromethane (5×3 mL). The product was separated by rotary evaporation at 35–40 °C and was recrystallised from ethanol and vacuum-dried for 5 h. It was identified by ^1H NMR in $CDCl_3$ solution with TMS as reference (300 MHz) and by FT-IR on a Shimadzu model 8201 PC spectrophotometer using the KBr pellet method.

3-(*N*-Phenylamino)-1,3-diphenyl-1-acetone: ^1H NMR (200 MHz, $CDCl_3$): $\delta=3.41$ (d, 2H), 4.93 (m, 1H), 6.48 (d, 2H), 6.59 (m, 1H), 7.01 (m, 2H), 7.18 (d, 1H), 7.24 (m, 2H), 7.35 (m, 5H), 7.85 ppm (d, 2H); IR: $\tilde{\nu}=3399$, 3024, 2974, 1672, 1598, 1515, 1295, 1221, 1080, 1026, 1001, 860, 693, 512 cm^{-1}.

3-(*N*-Phenylamino)-3-(3-chlorophenyl)-1-phenylacetone: ^1H NMR (200 MHz, $CDCl_3$): $\delta=3.42$ (m, 2H), 4.93 (m, 1H), 6.52 (d, 2H, $J=7.95$ Hz), 6.60 (m, 2H), 7.01 (m, 2H), 7.18 (m, 2H), 7.24 (d, 1H, $J=7.05$ Hz), 7.36 (d, 3H, $J=7.9$ Hz), 7.49 (m, 1H), 7.82–7.85 ppm (d, 2H, $J=7.8$ Hz); IR: $\tilde{\nu}=3390$, 3035, 1674, 1596, 1515, 1377, 1292, 1222, 1080, 1002, 929, 860, 749, 690, 621, 516 cm^{-1}.

3-(*N*-*p*-Bromophenylamino)-1,3-diphenyl-1-acetone: ^1H NMR (200 MHz, $CDCl_3$): $\delta=3.39$ (m, 2H), 4.87 (m, 1H), 6.34–6.38 (d, 2H, $J=7.9$ Hz), 7.06–7.10 (d, 2H, $J=8.25$ Hz), 7.16–7.25 (m, 3H), 7.29–7.34 (d, 2H, $J=9$ Hz), 7.37–7.41 (m, 2H), 7.47–7.50 (m, 1H), 7.80–7.85 ppm (d, 2H, $J=7.95$ Hz); IR: $\tilde{\nu}=3339$, 3020, 2937, 1675, 1509, 1485, 1367, 1308, 1273, 1119, 1072, 859, 753, 683, 518 cm^{-1}.

Claisen rearrangement reactions: These were carried out in batch mode in a three-necked round-bottomed flask (capacity 50 mL) under nitrogen atmosphere, using 3 g of allyl phenyl ether (APE) in 10 g of solvent (tetrachloroethylene, Loba Chemie) with 0.3 g of freshly calcined catalyst at 383 K. Aliquots of the reaction mixture were collected and analysed on a gas chromatograph fitted with an FID detector. The products were identified by gas chromatography–mass spectrometry (GC-MS) and gas chromatography–infrared spectroscopy (GC-IR).

Leaching and recyclability of the catalysts: To check for leaching of the TPA in the aforementioned reactions, the reactions were carried out for 1 h by using 15T-22.4TO-S15-1123 under selected reaction conditions. The reaction was stopped, the catalyst was separated by filtration from the hot reaction mixture, and the filtrate was stirred for 1 h under the same reaction conditions. In addition, tests for leaching of the TPA into the hot filtrate were carried out by inductively coupled plasma-optical emission spectroscopy. Before each cycle, the catalyst (15T-22.4TO-S15-1123) was washed three times with 1,2-dichloroethane, dried in an oven at 373 K for 24 h, and then activated for 4 h at 773 K in air. In the reactions with the recycled materials, the weight ratio of the catalyst to the reactants was kept constant.

Acknowledgement

D. P. Sawant thanks the NIMS for offering a NIMS postdoctoral researcher award.

[1] T. Okuhara, M. Misono, *CHEMTECH* **1993**, *23*, 23.
[2] T. Okuhara, N. Mizuno, M. Misono, *Adv. Catal.* **1996**, *41*, 113.
[3] H. Bosh, F. Janssen, *Catal. Today* **1988**, *2*, 369.
[4] G. C. Bond, S. F. Tahir, *Appl. Catal.* **1991**, *71*, 1, and references therein.
[5] G. Deo, I. E. Wachs, J. Haber, *Crit. Rev. Surf. Chem.* **1994**, *4*, 141, and references therein.
[6] M. Taramasso, G. Perego, B. Notari, US Patent, 4410501, **1983**.
[7] M. A. Vannice, R. L. Garten, *J. Catal.* **1979**, *56*, 236.
[8] J. C. Edwards, C. Y. Thiel, B. Benac, J. F. Knifton, *Catal. Lett.* **1998**, *51*, 77–83.
[9] A. Baiker, P. Dollenmeier, M. Glinski, A. Reller, *Appl. Catal.* **1987**, *35*, 351.
[10] H. M. Matralis, M. Ciardelli, M. Ruwet, P. Grange, *J. Catal.* **1995**, *157*, 368.
[11] R. Shafi, R. M. Sidiqui, G. J. Hutchings, E. G. Derouane, I. V. Kozhevnikov, *Appl. Catal. A* **2000**, *204*, 251.
[12] N. Essayem, Y. Been-Taarit, P. Y. Gayraud, G. Sapaly, C. Naccache, *J. Catal.* **2001**, *204*, 157.
[13] J. Pozniczek, A. Malecka-Lubanska, A. Micek-Ilnicka, A. Bielanski, *Appl. Catal. A* **1999**, *176*, 101.
[14] J. F. Knifton, J. R. Sanderson, *Appl. Catal. A* **1997**, *161*, 199.
[15] J. F. Knifton, *Appl. Catal. A* **1994**, *109*, 247.
[16] G. Kickelbick, *Prog. Polym. Sci.* **2003**, *28*, 83–114.
[17] E. Ortiz-Islas, T. López, R. Gómez, J. Navarrete, D. H. Aguilar, P. Quintana, M. Picquart, *Appl. Surf. Sci.* **2005**, *252*, 839–846.
[18] L. R. Pizzio, C. V. Cáceres, M. N. Blanco, *Appl. Surf. Sci.* **1999**, *151*, 91–101.
[19] N. Serpone, M. A. Jamieson, F. Isalvio, P. A. Takats, L. Yeretsian, J. R. Ufford, *Coord. Chem. Rev.* **1984**, *56*, 87–167.
[20] E. Ortiz-Islas, T. Lopez, R. Gomez, M. Picquart, D. H. Aguilar, P. Quintana, *Appl. Surf. Sci.* **2005**, *252*, 853–857.
[21] A. Popa, V. Sasca, E. E. Kiš, R. Marinković-Nedučin, M. T. Bokorov, J. Halasz, *J. Optoelectron. Adv. Mater.* **2005**, *7*, 3169–3177.
[22] C. T. Kresge, M. E. Leonowicz, W. J. Roth, J. C. Vartulli, J. S. Beck, *Nature* **1992**, *359*, 710–712.
[23] Q. Huo, D. Margolese, U. Ciesla, P. Feng, T. E. Cier, P. Sieger, R. Leon, P. Petroff, F. Schüth, G. D. Stucky, *Nature* **1994**, *368*, 317–321.
[24] U. Ciesla, S. Schacht, D. G. Stucky, K. Unger, F. Schüth, *Angew. Chem.* **1996**, *108*, 597–600; *Angew. Chem. Int. Ed. Engl.* **1996**, *35*, 541–543.
[25] P. V. Messina, M. A. Morini, M. B. Sierra, P. C. Schulz, *J. Colloid Interface Sci.* **2006**, *300*, 270–278.
[26] N. Enomoto, K. Kawasaki, M. Yoshida, X. Li, M. Uehara, J. Hojo, *Solid State Ionics* **2002**, *151*, 171–175.
[27] L. Zhao, J. Yu, *J. Colloid Interface Sci.* **2006**, *304*, 84–91.
[28] J. Yang, J. Zhang, L. Zhu, S. Chen, Y. Zhang, Y. Tang, Y. Zhu, Y. Li, *J. Hazard. Subst. Res.* **2006**, in press.
[29] T. E. Muller, M. Beller, *Chem. Rev.* **1998**, *98*, 675–704.
[30] Y. W. Li, T. J. Marks, *Organometallics* **1996**, *15*, 3770–3772.
[31] M. R. Douglass, M. Ogasawara, S. Hong, M. V. Metz, T. J. Marks, *Organometallics* **2002**, *21*, 283–292 (and references therein).
[32] A. Heutling, S. J. Doye, *Org. Chem.* **2002**, *67*, 1961 (and references therein).
[33] M. Kawatsura, J. F. Hartwig, *J. Am. Chem. Soc.* **2000**, *122*, 9546–9547.
[34] M. Lequitte, F. Figueras, C. Moreau, S. Hub, *J. Catal.* **1996**, *163*, 255–261.
[35] J. Horniakova, K. Komura, H. Osaki, Y. Kubota, Y. Sugi, *Catal. Lett.* **2005**, *102*, 191–196.
[36] M. Arend, B. Westermann, N. Risch, *Angew. Chem.* **1998**, *110*, 1096–1122; *Angew. Chem. Int. Ed.* **1998**, *37*, 1044–1070.
[37] B. List, P. Pojarliev, W. T. Biller, H. J. Martin, *J. Am. Chem. Soc.* **2002**, *124*, 827–833.
[38] B. List, *J. Am. Chem. Soc.* **2000**, *122*, 9336–9337.
[39] R. O. Duthaler, *Angew. Chem.* **2003**, *115*, 1005–1008; *Angew. Chem. Int. Ed.* **2003**, *42*, 975–978.
[40] K. Mogilaiah, G. Kankaiah, *Indian J. Heterocycl. Chem.* **2002**, *11*, 283–286.
[41] K. Manabe, Y. Mori, S. Kobayashi, *Tetrahedron* **2001**, *57*, 2537–2544.
[42] S. Kobayashi, T. Hamada, K. Manabe, *J. Am. Chem. Soc.* **2002**, *124*, 5640–5641.
[43] P. Desai, K. Schildknegt, K. A. Agrios, C. Mossman, G. L. Milligan, J. Aube, *J. Am. Chem. Soc.* **2000**, *122*, 7226–7232.
[44] M. Hiersemann, L. Abraham, *Eur. J. Org. Chem.* **2002**, 1461–1471.
[45] L. Claisen, *Chem. Ber.* **1912**, *45*, 3157–3166.
[46] a) F. E. Ziegler, *Acc. Chem. Res.* **1977**, *10*, 227–232; b) G. B. Bennett, *Synthesis* **1977**, 589–606.
[47] L. Y. Bryusova, M. L. Ioffe, *J. Gen. Chem.* **1941**, *11*, 722; [*Chem. Abstr.* **1942**, *36*, 430].
[48] a) W. Gerrard, M. F. Lappert, H. B. Silver, *Proc. Chem. Soc.* **1957**, 19–22; b) J. Borgulya, R. Medeja, P. Fahrni, H. J. Hansen, H. Schmid, R. Barner, *Helv. Chim. Acta* **1973**, *56*, 14–75.
[49] F. M. Sonnenberg, *J. Org. Chem.* **1970**, *35*, 3166–3167.
[50] K. Narasaka, E. Bald, T. Mukaiyama, *Chem. Lett.* **1975**, 1041–1044.
[51] W. Kuang, A. Rives, M. Fournier, R. Hubaut, *Appl. Catal. A* **2003**, *250*, 221–229.
[52] Y. Wu, X. Ye, X. Yang, X. Wang, W. Chu, Y. Hu, *Ind. Eng. Chem. Res.* **1996**, *35*, 2546–2560.
[53] R. I. Maksimovskaya, *Kinet. Katal.* **1995**, *36*, 836–843.
[54] Y. Kand, K. Y. Lee, S. Nakata, S. Asaoka, M. Misono, *Chem. Lett.* **1988**, 139–142.
[55] S. Uchida, K. Inumaru, J. M. Dereppe, M. Misono, *Chem. Lett.* **1998**, 643–644.
[56] D. Zhao, J. Feng, Q. Huo, N. Melosh, G. H. Fredrickson, B. F. Chmelka, G. D. Stucky, *Science* **1998**, *279*, 548–552.
[57] N. Chino, T. Okubo, *Microporous Mesoporous Mater.* **2005**, *87*, 15–22.
[58] B. H. Davis, R. A. Keogh, S. Alerasool, D. J. Zalewski, D. E. Day, P. K. Doolin, *J. Catal.* **1999**, *183*, 45–52.
[59] S. M. Kumbar, G. V. Shanbhag, F. Lefebvre, S. B. Halligudi, *J. Mol. Catal. A: Chem.* **2006**, *256*, 324–334.
[60] Y.-L. Lin, T.-J. Wang, Y. Jin, *Powder Technol.* **2002**, *123*, 194–198.
[61] H. Chermette, G. Hollinger, P. Pertosa, *Chem. Phys. Lett.* **1982**, *86*, 170–175.
[62] C. Rocchiccioli-Deltcheff, M. Fournier, R. Franck, R. Thouvenot, *Inorg. Chem.* **1983**, *22*, 207–216.
[63] M. Hartmann, S. Racouchot, C. Bischof, *Microporous Mesoporous Mater.* **1999**, *27*, 309–320.
[64] K. Schumacher, M. Grün, K. K. Unger, *Microporous Mesoporous Mater.* **1999**, *27*, 201–206.
[65] D. Zhao, J. Sun, Q. Li, G. D. Stucky, *Chem. Mater.* **2000**, *12*, 275–279.
[66] H. P. Klug, L. E. Alexander, *X-ray Diffraction Procedures*, Wiley, New York, **1974**.
[67] G. D. Yadav, S. V. Lande, *J. Mol. Catal. A* **2006**, *243*, 31–39.
[68] N. T. Mathew, S. Khaire, S. Mayadevi, R. Jha, S. Sivasanker, *J. Catal.* **2005**, *229*, 105–113.
[69] Á. Molnár, T. Beregszászi, Á. Fudala, P. Lentz, J. B. Nagy, Z. Kónya, I. Kiricsi, *J. Catal.* **2001**, *202*, 379–386.

Received: October 5, 2007
Published online: February 21, 2008

